

Dissipative quantum coherent dynamics probed in phase-space: Electronically resonant 5-color 4-wave mixing on I₂(B) in solid Kr

D. Segale^{a)} and V. A. Apkarian^{b)}*Department of Chemistry, University of California, Irvine, California 92697-2025, USA*

(Received 24 March 2011; accepted 18 May 2011; published online 8 July 2011)

Spectrally resolved, 4-wave mixing measurements in five resonant colors are used to interrogate vibronic quantum coherences in phase-space. We highlight the principles through measurements on the B-state of I₂ in solid Kr – a prototype of a system strongly coupled to its environment. The measurements consist of preparing a superposition of wavepackets on the B-state and interrogating their cross-coherence as they get entangled with the environment. The study provides direct realizations of fundamental quantum principles in the mechanics of molecular matter, among them: the distinction between quantum and classical coherent dynamics of a system entangled with the environment, coherent dissipation, event-driven decoherence, environment selected coherent states, and non-local mechanics. © 2011 American Institute of Physics. [doi:10.1063/1.3598959]

I. INTRODUCTION

To interrogate the quantum coherence of vibronic wavepackets, measurements that distinguish between diagonal and off-diagonal densities (population versus coherence) are invaluable. We have previously implemented electronically resonant four-wave mixing (ERFWM) as such a tool.¹ Be it in time or frequency domain, a large number of phenomena can be interrogated through four-wave mixing (FWM).² Our ERFWM measurements are illustrated in Fig. 1. They are designed as a two-slit experiment in which a superposition of two vibrational wavepackets are prepared on an electronically excited state, and their amplitude level cross-correlation is probed by coherent Raman scattering via a third electronic state. The signal probes the off-diagonal density; namely, the vibrational coherence as a function of initial preparation conditions, and the course of decoherence of a system that is strongly coupled to its environment. The implementation is on the prototypical system of I₂(B) isolated in solid Kr, about which a wealth of information already exists.³ We show that spectrally resolved, multi-color FWM with independently controlled timings, colors, and pulse characteristics of the three input beams, allow a detailed exploration of vibrational coherences in phase space.⁴ Previously, we reported on such measurements in the context of the preparation and detection of “cat”-states.¹ Here, we outline the phase-space information accessible in such measurements and highlight fundamental principles regarding quantum coherent mechanics that can be elucidated.

Typical of molecular matter, when I₂ trapped in rare gas solids is suddenly prepared on electronically excited states, wavepacket motion is observed through pump-probe (pu-pr) measurements.⁵ In contrast with complex systems, ranging from biomolecules to solid and liquid solutions in which wavepacket motion is observable, I₂ trapped in rare gas solids

is sufficiently well characterized to lend itself to explicit atomistic interpretations, and in particular to semi-classical simulations that most directly relate to quantum many-body dynamics.^{6–8} Early on, simulations were used to demonstrate that fluorescence detected pump-probe signals could be reproduced through strictly classical dynamics.⁹ Classical simulations also reproduce wavepacket control with chirped pulses, when using initial conditions that reflect the optical preparation while propagating trajectory ensembles in a simulation cell containing 10²–10³ atoms.¹⁰ The inference is that pump measurements track the coherent evolution of the classical reduced density $\rho_c(t)$. Thus, for an impulsively prepared wavepacket, prepared in short enough time to preclude environmental response during preparation, the global wavefunction may be factorized as the product of system (*s*) and bath (*b*):^{11,12}

$$|\Psi(0)\rangle = |\varphi\rangle^{(s)} |\Phi\rangle^{(b)}, \quad (1)$$

coupled quantum evolution in the tensor space $s \otimes b$ produces the density

$$\rho = |\Psi\rangle\langle\Psi| = \rho_c + \sum_{n \neq m} \sqrt{p_n p_m} |\varphi_n\rangle\langle\varphi_m| \otimes |\phi_n\rangle\langle\phi_m|. \quad (2)$$

in which the classical density ρ_c consists of the ensemble of correlated states:

$$\rho_c = \sum_n p_n |\varphi_n\rangle\langle\varphi_n| \otimes |\phi_n\rangle\langle\phi_n|, \quad (3)$$

while the interferences in (2) represent the quantum coherence. Since projective measurements on the system trace out the bath,

$$\langle P \rangle = \text{Tr}_b[\hat{P}\rho], \quad (4)$$

the observable density collapses into (3). In this von Neumann interpretation of measurements, $|\phi_n\rangle\langle\phi_n|$ represent the pointer states of a classical measuring device.¹³ The interpretation also suggests decoherence as the collapse

^{a)}Present address: Illumina Inc., San Diego, California 92121, USA.

^{b)}Author to whom correspondence should be addressed. Electronic mail: aapkaria@uci.edu.

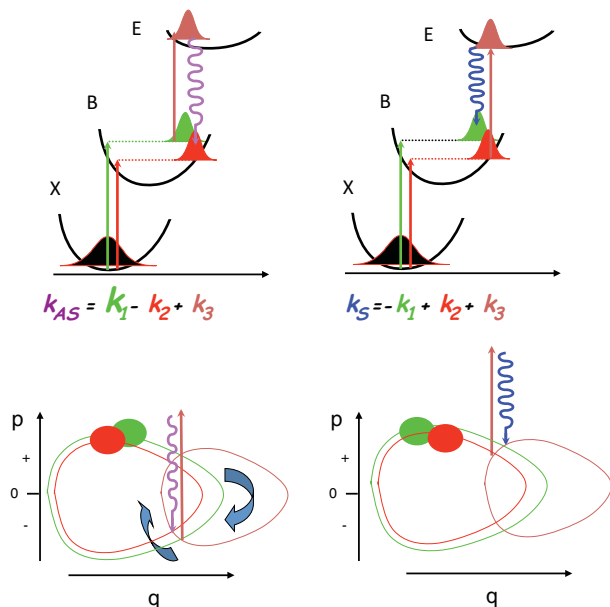


FIG. 1. The measurement: (a) (top panel) time circuit diagrams overlaid on the molecular potentials show the preparation of two packets on the B-state, and interrogation via coherent Raman scattering between the two packets; (b) (bottom panel) phase-space representation of the electronically resonant process highlights that the time-ordered correlation leads to selective scattering. For $\varepsilon_1 > \varepsilon_2$, AS- and S-scattering occur at p^- and p^+ momentum branches, respectively.

to classicality due to the system being measured by its environment.^{14,15} Since in pump-probe measurements the signal is proportional to population resonantly transferred to a radiative final state, $\hat{P} = \hat{\mu}|f\rangle\langle f|\hat{\mu}$, the observable is reduced to the diagonal classical coherence (3). One is left to wonder about the extent of quantum coherence and its fate. That this is non-negligible has been demonstrated through interferometric measurements in closely related studies of dihalogens in rare gas matrices.^{16,17} Coherence of the coupled chromophore bath is interrogated,¹⁸ and phase controlled.^{19,20}

The present measurement paradigm is illustrated in Figure 1 with time-circuit diagrams overlaid on the schematic system potentials. A superposition of two wavepackets is prepared on the B-state of the molecule using two non-collinear laser pulses:

$$|\Psi(0)\rangle = (|\varphi_1\rangle + |\varphi_2\rangle)^{(s)} |\Phi\rangle^{(b)}. \quad (5a)$$

Coupled evolution in time leads to the entangled system-bath state

$$|\Psi(t)\rangle = |\varphi_1'\rangle^{(s)} |\phi_1\rangle^{(b)} + |\varphi_2'\rangle^{(s)} |\phi_2\rangle^{(b)}, \quad (5b)$$

where the primes indicate that the initial system packets have exchanged energy and phase with the environment.²¹ A time-delayed probe pulse, resonant with the $E(0_g)$ ion-pair state, is then used to induce coherent Raman scattering between the two excited state packets. The measurement consists of creating phase-space overlap between the two packets after a short-time evolution on the E-state to connect the Franck-Condon intersections (see Fig. 1(b)). Overlap in phase space (p, q) of the system alone is not sufficient to observe coherent radiation. The generation of coherent radiation from the third-order polarization is contingent upon amplitude level correla-

tion between the entangled states:

$$\rho_{12}^{(s)} = \sqrt{p_1 p_2} (|\varphi_1'\rangle \langle \varphi_2'\rangle)^{(s)} \langle \phi_1 | \phi_2 \rangle^{(b)}. \quad (6)$$

The coherence survives only if the packets share or create a common bath, $\langle \phi_1 | \phi_2 \rangle^{(b)} \neq 0$. Decoherence arises from the difference in action exerted by the packets on the bath, $\langle \phi_1 | \phi_2 \rangle_t^{(b)} = e^{i(S_1 - S_2)} \rho_b$, with formal measure given in terms of the Loschmidt echo.^{22–25} While individually each packet may have a different influence on the bath, non-locality provides for communication between them through the bath, and therefore common (non-local) action of the superposition on the environment. This requirement for coherent dissipation can be clearly demonstrated in the measurements to be reported. The prior pump-probe studies have established the dissipative mechanics of packets when individually prepared on I_2/Kr . It has been shown that vibrational energy transfer from the molecule to the lattice varies by three orders of magnitude in the first period of motion in the 580 nm – 480 nm excitation range.²⁶ We will take advantage of this tunability of coupling strength between system and environment to interrogate non-trivial quantum coherences. We should note from the onset that in this limit of strong coupling, the system does not sustain vibrational eigenstates. The spectrum of I_2 in Kr does not contain vibrational structure – the evolution is in a vibrational continuum. As such, the natural basis for states is in energy representation, $\rho(\varepsilon, \varepsilon')$, and the phase space representation $\rho(p, q; t)$ is the preferred description of the evolving dynamics.²⁷

II. EXPERIMENTAL

The experiments are carried out on thin films of I_2 doped Kr, formed by depositing a premixed sample at a dilution ratio of 1:4000 on a sapphire window held at 32 K using a closed cycle cryostat. The laser system used consists of a commercial pump source (Clark MXR-1000) operating at $\lambda = 775$ nm, with 800 mW output power at a repetition rate of 1 kHz, and a pulse width of ~ 200 fs. The laser is used to pump three home-built non-collinear optical parametric amplifiers (NOPA), which have been previously described. Using a two-prism (SF-10) compressor, pulses as short as 20 fs can be obtained. To stretch the pulses, we introduce group velocity dispersion in the white-light arm of the NOPA by inserting quartz optical flats. The stretched pulses are typically 100 fs wide, and 1.5 times the transform limit, as determined through frequency-resolved optical gating. Delay lines control the timing among the three beams obtained from the three different NOPAs, which are brought together into focus on the sample using a single achromatic lens ($f = 10$ cm) in the box-car geometry, as illustrated in Figure 2. The initial alignment of the three beams is carried out on a glass substrate, and the optical trains are tuned to ensure multiple order scattering (see Fig. 2) prior to the measurements. Two fibers are used to simultaneously collect the spatially distinct third-order polarizations, $P_{AS}^{(1,2)}$ and $P_S^{(2,1)}$, propagating along

$$k_{AS} = k_3 + (k_1 - k_2) \quad \text{and} \quad k_S = k_3 + (k_2 - k_1), \quad (7)$$

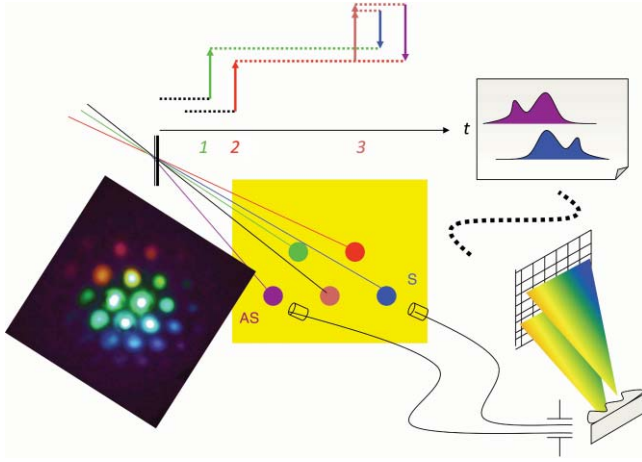


FIG. 2. Experimental scheme: three non-collinear pulses, in three different colors are used. The directional AS-/S-polarizations are simultaneously collected with fibers. They are dispersed in a monochromator and the spectra are simultaneously recorded on a 2-D CCD array. The phase matching is accomplished on glass, by optimizing for high order scattering, as in the photographed image shown.

with corresponding energy conservation conditions:

$$\omega_{AS} = \omega_3 + (\omega_1 - \omega_2) \quad \text{and} \quad \omega_S = \omega_3 + (\omega_2 - \omega_1). \quad (8)$$

We adhere to the convention:

$$\omega_1 > \omega_2, \quad (9)$$

hence the designation of S- and AS- for the two polarizations. Measurements are carried out as a function of delays t_{21} and t_{31} , with the simultaneous recording of the spectra of the two polarizations through a 1/4-meter monochromator, using a CCD array binned vertically into two segments. By opening the limiting apertures used for spatial filtering, the pump-probe induced fluorescence signal from the molecular ion-pair states is recorded along with the third order polarizations. Note, the experimental arrangement is identical to that used in coherent anti-Stokes Raman spectroscopy (CARS) measurements on the ground electronic state of the molecule, which can be seen at long probe wavelengths that are not resonant with the ion-pair state.²⁸ The two-orders of magnitude difference between the B-E charge transfer transition versus the B-X valence transition ensures that excited state FWM completely overwhelms CARS on the X-state.

III. RESULTS AND ANALYSIS

A large number of multi-dimensional, multi-color measurements have been carried out to clarify the principles of the nonlinear optical response and to sort out the systematics of the material coherence subject to various initial preparations.⁴ We use a set selected to illustrate the information that can be readily read-out from the data and that contains clear lessons regarding coherence in strongly coupled dissipative systems.

A. Coherence in the spectral coordinate

An example of five-color four-wave mixing measurements is given in Figure 3. We provide simultaneously

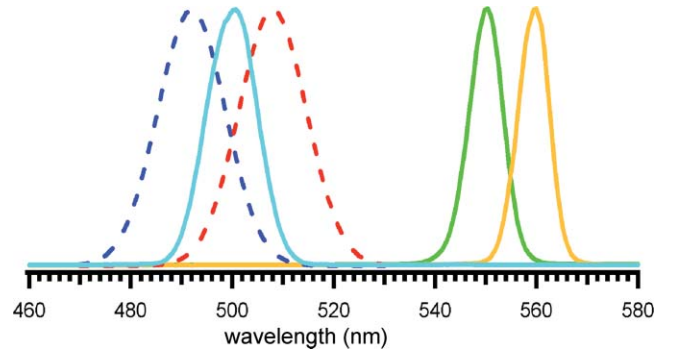


FIG. 3. The spectra of the three input pulses used in narrow-band four-color measurements (solid lines) and the non-resonant S- and AS-spectral windows (dashed red and blue, respectively) that arise by their triple convolution. The pulses are centered at $\lambda_1 = 550$ nm, $\lambda_2 = 560$ nm, and $\lambda_3 = 500$ nm, with fwhm $\Delta\lambda_1 = 8$ nm, $\Delta\lambda_2 = 7$ nm, and $\Delta\lambda_3 = 12$ nm and pulse widths of $\Delta\tau_1 = 95$ fs, $\Delta\tau_2 = 105$ fs, and $\Delta\tau_3 = 60$ fs.

recorded AS-/S- spectra as a function of probe delay, t_{31} , for fixed $t_{21} = -30$ fs, selected to optimize the signal at first recursion. The spectral composition of pulses and their characteristics are summarized in Figure 3. Given spectral distributions, the energy conservation condition (8) defines the signal windows through the triple convolution (see Fig. 3):

$$I_{nr}^{(3)}(\omega) = \int_0^\infty d\omega'' I_3(\omega - \omega'') \int_0^\infty d\omega' I_2(\omega\omega' - \omega'') I_1(\omega\omega'). \quad (10)$$

This is the instantaneous, non-resonant coherent response, which can be observed in glass when all three input pulses coincide and is used in the procedure of alignment. To the extent that the optical coherence is transferred to the material, the energy conservation condition (8) may be re-stated in terms of the energies of the packets:

$$\hbar\omega_{12} = \hbar\omega_3 + (\varepsilon_1 - \varepsilon_2)_t \quad \text{and} \quad \hbar\omega_{21} = \hbar\omega_3 - (\varepsilon_2 - \varepsilon_1)_t, \quad (11)$$

with time dependent mean energy associated with each packet $\bar{\varepsilon}_i(t) = \langle \varphi_i(t) | H | \varphi_i(t) \rangle$ due to dissipation. The spectral representation equivalent of (10), becomes

$$I_{res}^{(3)}(\omega; t) = \int_0^\infty d\varepsilon I_3(\hbar\omega - \varepsilon) \int_0^\infty d\varepsilon' \rho_2(\varepsilon' - \varepsilon) \rho_1(\varepsilon'). \quad (12)$$

It is determined by the convolution of the probe laser spectrum with the coherence width in energy. If we coarse grain the time by integrating (12) over a cycle, then the spectrum provides a direct readout of $(\bar{\varepsilon}_2 - \bar{\varepsilon}_1)_t$, namely the anti-diagonal of the density in energy representation $\rho(\varepsilon_1, \varepsilon_2)$. In Fig. 3, the probe laser spectrum can be observed at negative time, due to a weak permanent volume grating that is formed after extended irradiation of the solid. At $t = 0$, when the bath has not had the chance to evolve, the signal spans the full non-resonant window. A narrower spectrum is seen upon first recursion, followed by gradual spectral collapse accompanied by the sliding of the spectral peak toward degeneracy.

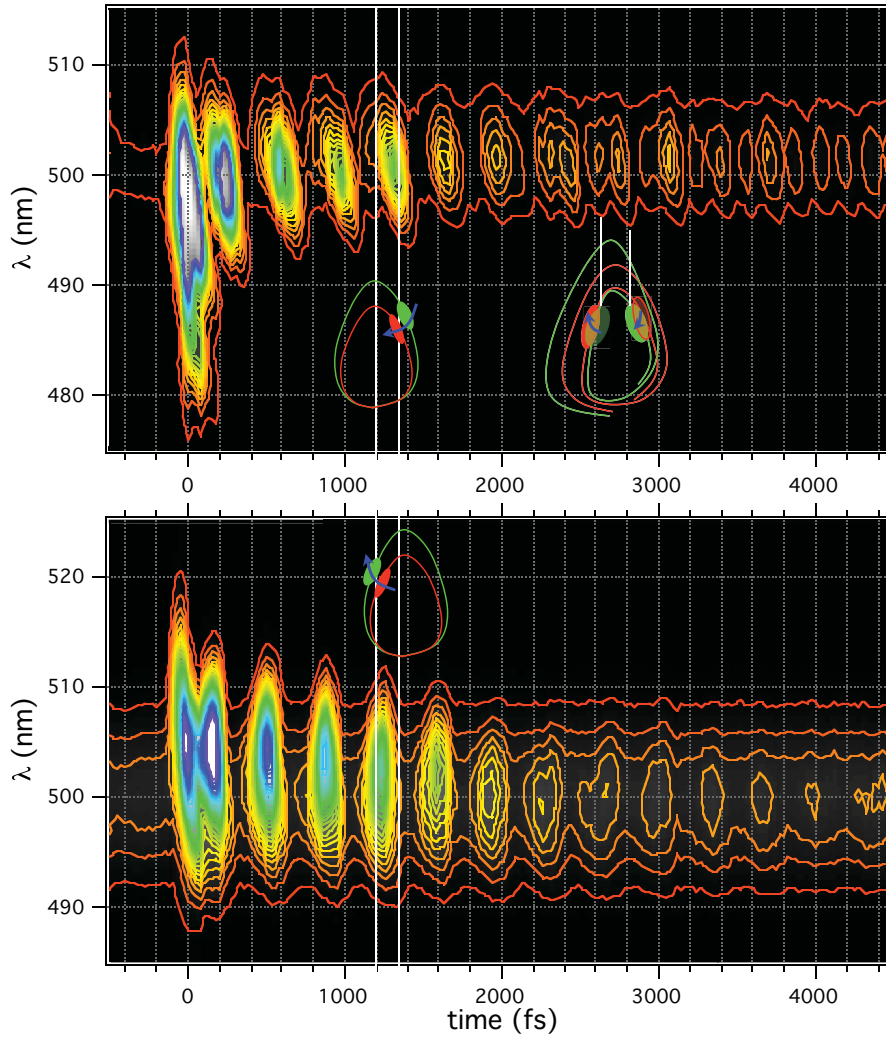


FIG. 4. Simultaneously recorded S- and AS-scattered spectra in the five-colors shown in Fig. 3, as a function of probe delay t_{31} , for fixed $t_{21} = -30$ fs. The two vertical lines in the fifth period correspond to p^+ and p^- intersections.

By the fifth cycle of motion (marked by two vertical lines in Fig. 4), the limiting spectrum of the probe pulse is reached, i.e., the limit at which the coherence reduces to the diagonal density, $\bar{\varepsilon}_2 - \bar{\varepsilon}_1 \rightarrow 0$. The vibrational energies of the packets and their distributions, which define the diagonal of the coherence $(\varepsilon_2 + \varepsilon_1)_t/2$ in the $\varepsilon_1, \varepsilon_2$ -plane, will be extracted below from the analysis of recursion periods.

B. Differential scattering between k-vector tagged packets

The counter-phase timing of the S- and AS-signals is more clearly highlighted by the spectral cuts shown in Fig. 5. The anti-correlation is the outcome of the real electronic resonance used in the measurement, which determines the distinct phase-space paths over which the coherent Raman scattering takes place. As illustrated in Fig. 1, $P_{AS}^{(1,2)}$ arises by promoting φ_1 to the E-state and evolution there until reaching overlap with φ_2 . With the definition $\hat{P}_{2 \leftarrow 1} \equiv \int d\tau e^{iH_B\tau/\hbar} \hat{\rho} e^{-iH_E\tau/\hbar} \hat{\rho} E_3$, the projective measurement (4) can be understood to involve a translation in phase space to

create overlap,

$$P_{AS}^{(1,2)} = \hat{P}_{2 \leftarrow 1}(q_2, p_2, t_4 \leftarrow q_1, p_1, t_3) |\varphi_1\rangle \langle \varphi_2|, \quad (13a)$$

while

$$P_S^{(2,1)} = \hat{P}_{1 \leftarrow 2}(q_1, p_1, t_4 \leftarrow q_2, p_2, t_3) |\varphi_2\rangle \langle \varphi_1|. \quad (13b)$$

The Franck-Condon condition, $\delta[q_B - q_E, p_B - p_E]$, is fulfilled at the intersections of the phase space trajectories on the B- and E-states. The initial coordinates, q_i , at which the packet may be intercepted is dictated by the difference potential

$$\hbar\omega_3 = \Delta V_{BE}(q_i) = V_E(q_i) - V_B(q_i), \quad (14a)$$

with associated momenta that are double-valued: p_i^+ and p_i^- . The observation of one recursion per period (initial 2 ps in Fig. 4) indicates that only one momentum branch contributes to each scattering channel. Their timing, S- preceding AS- by 90 fs (spacing between vertical lines in Fig. 4) and periodicity of 350 fs, identifies the intercepted branches as p_i^+ and p_i^- , respectively. Single branch scattering is the consequence of fast electronic dephasing between B and E states.²⁹ Thus, for $\varepsilon_1 > \varepsilon_2$, the time ordered correlation $\varphi_1 \rightarrow \varphi_E \rightarrow \varphi_2$ starting at p_i^+ requires a full cycle on the E-state, in

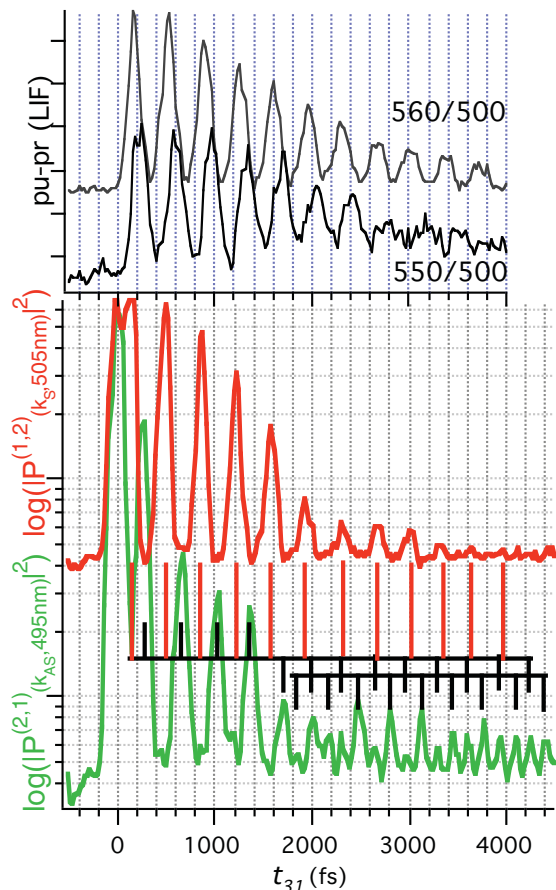


FIG. 5. Semilogarithmic spectral cuts taken at 495 nm and 505 nm from the AS- and S-signals (bottom panel) of Fig. 4, along with the pump-probe induced fluorescence signal (top panel). The markers show the slippage of phase between the two scattering channels, and the appearance of period doubling in the AS-signal.

contrast to the short path when starting at p_i^- . The absence of spectral modulation in the detected signal establishes that the E-B electronic dephasing time is shorter than the E-state period. Period halving can be seen in the degenerate window for $t > 2$ ps in Fig. 4 (top). Now scattering at both p^+ and p^- contributes to a given channel, which is possible only for packets that overlap in energy: $\varepsilon_1 = \varepsilon_2$. After dissipation, past the fifth cycle, the modulated signal that appears on a zero-background is the cross-coherence between packets that overlap in energy. Although they overlap in energy, their identities are preserved by the k-vectors in the macroscopic sample: S- and AS- scattering remains directional (7). The distinguishability of paths along the system coordinate allows mechanistic (causal) assignments to individual packets, while the action of the superposition on the bath leads to the quantum inseparability, inherent in a two-slit experiment.³⁰

The color of the detected polarization identifies the final scattering coordinate, q_f ,

$$\hbar\omega_4 = \Delta V_{BE}(q_f) = V_E(q_f) - V_B(q_f), \quad (14b)$$

with associated final momentum branches that can be inferred from the interception time of the packets. While FC windows define the allowable transition coordinates, the sampling is controlled by the synchronization of pulses: t_{31} controls the

intercepted slice of p_i , q_i , and t_{21} dictates the accessible final coordinates (p_f , q_f , $t_4 \leftarrow p_i$, q_i , t_3) that can be connected along the E-state trajectory during t_{43} . This conditional scattering probability can be expressed for frozen Gaussian packets,

$$S(\omega_3, \omega_4) = e^{-[q_2(t_{31}-t_{21})-q_f]/\Delta q_2]^2} e^{-[q_1(t_{31})-q_i]/\Delta q_1]^2} \times e^{-[p_1(t_{31})-p^-]/\Delta p_1]^2}, \quad (15)$$

using a suitable pair of trajectories to represent the packets. The expression is meant to interpret the timing between the launching and detection of signals at different colors (see below). It does not address any details of the underlying dynamics, an exact treatment of which is inaccessible.

C. Coherent dissipation in a driven common bath

In Fig. 5, we present semilogarithmic cuts taken from the λ, t -map of Fig. 4 (AS- at 495 nm and S- at 505 nm), along with the pu-pr induced fluorescence over the $D'' \rightarrow A''$ transition at 325 nm (top panel). At the probe wavelength of 500 nm, both packets remain within the FC window for the duration of their life on B. The observed uneventful decay of the pu-pr signal is controlled by predissociation, which occurs with a time constant of ~ 2 ps.^{31,32} The S-signal envelope shows an initial Gaussian decay, characteristic of inertial evolution, followed by drops in signal intensity at $t = 1.8$ ps and then again at $t = 3.2$ ps. These features are magnified in the AS-signal. The latter shows an abrupt drop in intensity by a factor of 3 after the first period, followed by exponential decay for three cycles, a second abrupt three-fold drop at $t = 1.6$ ps, and then again at $t = 3.2$ ps. These punctuated drops in coherence are absent in the pu-pr data – they cannot be mistaken with population decay. They indicate event-driven decoherence. The events coincide with the step-wise loss in amplitude of the classical trajectory shown in Fig. 6, which is from molecular dynamics simulations previously used to reproduce pu-pr signals with good fidelity.¹⁰ The stars indicate the cage-molecule collisions, which can therefore be identified as the events that punctuate the observed decoherence.

Inspection of the AS-slice in Fig. 5 (bottom) is informative. Initially, it shows one recursion per period, arising from interception of φ_1 at p^- , consistent with the preparation condition $\varepsilon_1 > \varepsilon_2$. Past $t = 1.6$ ps, scattering at both momentum branches leads to period halving, indicating that now $\varepsilon_1 = \varepsilon_2$. Past $t = 2.2$ ps the contribution from p^+ becomes larger than that at p^- ; now the coherence is limited to the density where $\varepsilon_1 < \varepsilon_2$, even though initially φ_1 was prepared above φ_2 by $\hbar\omega_1 - \hbar\omega_2 = 325 \text{ cm}^{-1}$. The implicit nonlinear dissipation is also evident in the slippage in recursion times between the two scattering channels, as indicated by the markers in Fig. 5 (bottom). In the first cycle, the AS-signal is delayed relative to the S-signal by 170 fs, they catch-up on the seventh cycle, and the AS-signal advances relative to the S-signal in subsequent cycles by ~ 50 fs. Clearly, the coherence is that of a dissipative packet in an anharmonic potential, which is coupled to the lattice.

The course of dissipation in an anharmonic potential can be followed through the time course of recursions. In

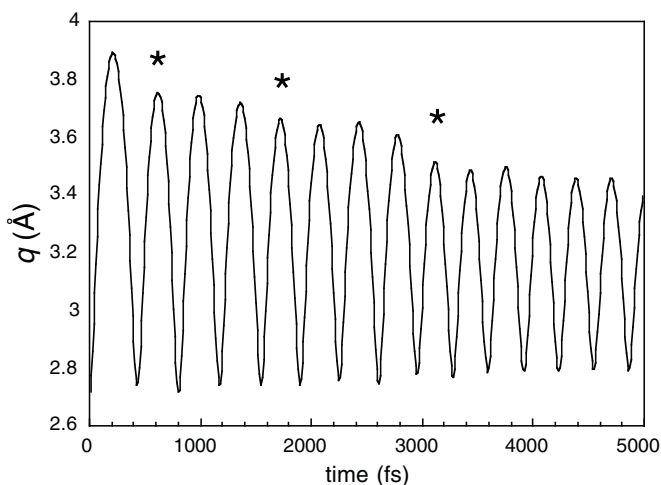


FIG. 6. A representative trajectory from molecular dynamics simulations of I_2/Kr (Ref. 10). The damping of the amplitude of the oscillator is modulated by the cage motion, with cage-molecule collisions identifiable at the step jumps marked by the stars. These steps are perfectly correlated with the drop in the AS-scattering intensity seen in Fig. 4.

Figure 7, we collect the observed periods, $t_{n+1}-t_n$, as a function of cycles for different spectral cuts, along with the pu-pr data. The scatter is expected for an oscillator coupled to the bath, as previously demonstrated through simulations. On the right ordinate of Fig. 7, we provide the translation of periods to vibrational energy assuming a Morse potential, $E_v = D_e(1 - \omega^2/\omega_e^2)$, with previously determined parameters.³³ Note, the initial preparation is at $E_v = 2750 \text{ cm}^{-1}$ (550 nm) where the expected Morse period would be 475 fs. Yet the first mean period in Fig. 7 is 360 fs – already after the loss of $\sim 1000 \text{ cm}^{-1}$ in vibrational energy. The general trends seen in Fig. 7 agree with prior pu-pr determinations.³⁴ The notable difference in the present is the interweaving of the AS- and S-periods, which clock φ_1 and φ_2 , respectively. In one cycle, φ_1 loses $\sim 300 \text{ cm}^{-1}$

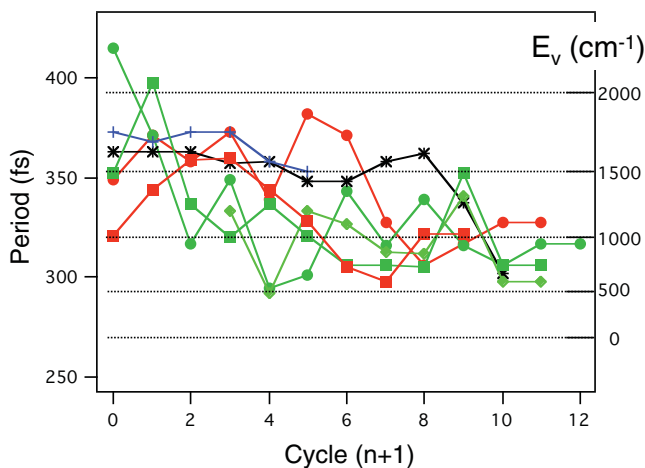


FIG. 7. Recursion periods, $t_{n+1}-t_n$ as a function of cycle number n , obtained from: AS-signal (green) at 500 nm (squares) and at 495 nm (circles) including the recursions after period doubling; S-signal (red) circles at 500 nm (squares) and at 505 nm (circles); LIF data for individually prepared packets at 550 nm (blue) and at 560 nm (black). The right ordinate relates period to vibrational energy assuming a Morse potential.

in energy, while φ_1 gains $\sim 300 \text{ cm}^{-1}$. φ_1 continues to lose energy, shedding $\sim 1400 \text{ cm}^{-1}$ by the fifth cycle. In contrast, φ_2 gains $\sim 600 \text{ cm}^{-1}$ during the first four cycles, then trails the dissipation course of φ_1 . Past the seventh period they reach a common limit, with fluctuations in period that correspond to an energy spread of $\sim 300 \text{ cm}^{-1}$, comparable to the spread in the initial preparation. During the first four cycles, the superposition consists of a φ_1 wave that spirals down in energy and a φ_2 wave that spirals up: the molecule simultaneously loses and gains energy.

The greater energy loss of φ_1 is consistent with the fact that individually prepared packets in the more anharmonic region of the potential lose larger energy upon collision with the cage. The more intriguing observation is period elongation, which suggests energy gain. Such period elongation has been observed in I_2 isolated in ice.³⁵ It occurs when vibrations adiabatically follow a slowly dilating cage. This process is not seen for individually prepared packets on $I_2(B)/Kr$. In the present case, the cage dilation is driven by the extension of the molecular bond – work done by the outgoing packet. The data suggests that the work of cage expansion is borne by φ_1 , while φ_2 follows the driven, dilating cage. Seemingly, the coherence is between two packets that communicate through a common bath. That the effect is non-classical, can be recognized by the consideration that it cannot be simulated with an ensemble of independent trajectories. Nonlocality is the hallmark of wave mechanics, which is required for quantum coherent dissipation (6). The present realization seems a particularly direct demonstration in molecular mechanics.

D. Decoherence in energy representation

The most direct basis for sorting the observable coherence is in the energy representation. The spectrum directly measures the off-diagonal energy distribution along $\varepsilon_{12} = \varepsilon_1 - \varepsilon_2$. For energy densities with normal distributions around means, $\bar{\varepsilon}_2$ and $\bar{\varepsilon}_1$, the spectral peak provides the separation of the coherence center from the energy diagonal $\langle \varepsilon_{12} \rangle_t = \varepsilon_1 - \varepsilon_2$, while a suitable choice of a contour line provides the width $\Delta \langle \varepsilon_{12} \rangle_t$, after correcting for spectral convolution with the probe pulse. To determine the diagonal energy distribution, we rely on the observed periods and their dispersion (Fig. 7). The reconstructed coherence map, $\rho(\varepsilon_1, \varepsilon_2)$, is shown in Figure 8 for the first third and fifth recursions of the AS-signal, along with the vibrational state grid that discretizes the energy basis. While initially the coherence is prepared with an energy spread of 300 cm^{-1} , by the first recursion it slides to $\langle \varepsilon_{12} \rangle = 150 \text{ cm}^{-1}$, and by the fifth cycle it is limited to the diagonal. Nevertheless, the periodic coherent wavepacket motion continues to be visible both in FWM and in pu-pr measurements. In this nearly classical limit, the density maps onto ~ 4 vibrational states (Fig. 8), with coherence limited to nearest neighbors.

Timescales may be associated with the observed decoherence by forcing exponential fits to spectral cuts and correcting for predissociation. Thus, at the degenerate wavelength of 500 nm, the $P^{(1,2)}$ and $P^{(2,1)}$ time constants are 0.7 ps and 1.1 ps, to be compared with the decay due to predissociation

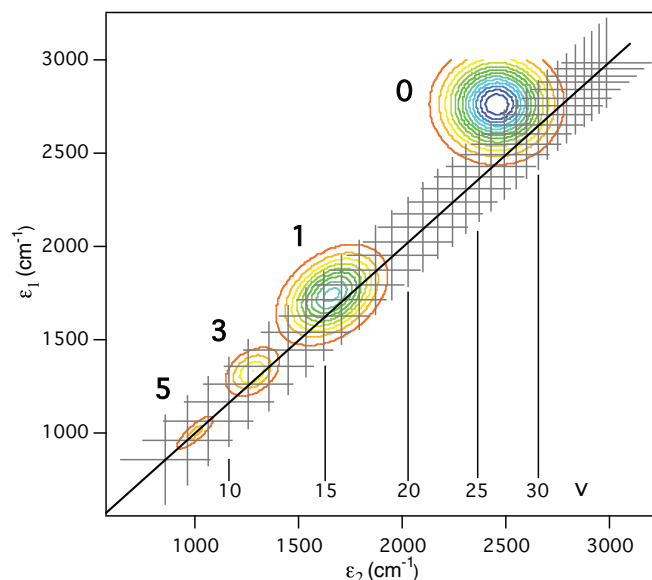


FIG. 8. Reconstruction of the time-dependent coherence in energy representation for the data in Fig. 3. The initially prepared coherence (0) dictated by the laser pulses; and three subsequent distributions obtained from the first, third, and fifth recursions at 0.2, 1, and 1.6 ps of the AS-scattering in Fig. 4. The diagonal energies and spreads are obtained from the period analysis in Fig. 6, while the off-diagonal widths are from the spectral shift and width of the recursions in Fig. 4. The provided vibrational grid is artificial, the system does not sustain vibrational eigenstates – the spectrum of the oscillator is continuous.

of $\tau_p/2 = 0.9$ ps and 1.3 ps for packets separately prepared at 550 nm and 540 nm. The decay of the coherent signal is quite comparable to that of the population. At non-degenerate wavelengths, decoherence times shorten linearly with energy separation over the measurable range of $0 < |\varepsilon_2 - \varepsilon_1| < 800$ cm^{-1} , with a dependence $\tau/|\varepsilon_2 - \varepsilon_1| = -1.25$ fs/cm^{-1} . This coarse grain analysis shows the rate of decoherence to be linear in energy separation. The coherence within the degenerate window lasts nearly as long as the population. In essence, packets that survive to reach coherent overlap in phase space suffer a similar subsequent history in the bath.

E. Synchronization between packets

By controlling the delay between the launching times of the packets, the signal can be coerced from different FC-accessible regions. The data in Fig. 3 were obtained for $t_{21} = -30$ fs, with φ_2 retarded to compensate for anharmonicity. In Fig. 9, we show the case for φ_2 launch advanced by $t_{21} = 70$ fs. Now, the AS-signal shows a packet as it turns around the outer corner of the potential with near zero momentum, while the period-halved S-signal captures a packet with large momentum, once on each momentum branch. The synchronization that leads to these signals (marked as 1-4 in Fig. 9) can be understood with the help of the classical packets shown in Figure 10. The weak red-shifted AS-signal at p^+ , marked as 2 in Figs. 9 and 10, arises from the overlap of the advancing edge of φ_1 with the trailing edge of φ_2 . This scattering is only possible because of the overlap in energy of the packets, due to the spectral overlap of the pulses that prepare them. The AS-signal that arises from $p^+ \leftarrow p^-$ crossover scattering

is marked as 4 in Figs. 9 and 10. After φ_1 is intercepted in the p^- window, evolution on the E-state allows enough time for φ_2 to catch-up, to create optimal overlap of final states. The early S-signal, marked as 1 in Figs. 9 and 10, arises from the same head-tail overlap as the weak S, but is significantly more intense, since it is not limited to the density that overlaps in energy. The turning of the corner is continuously tracked (marked 1-3 in Figs. 9 and 10), with scattering taking place around the closed loop between B- and E-trajectories. Again crossover scattering between the two momentum branches is a significant contribution. At the corner where the packets are nearly stationary, the polarizations arising from the two FC intersections between B- and E-states should interfere. This is evident by the sharp dividing line that bisects the corner.

In many important aspects, the event driven decoherence dynamics remains the same as in the case of the coincident packets (compare Figs. 11 and 5). A noteworthy difference is that now the S-signal also shows an abrupt drop in intensity after the first recursion (Fig. 11) in contrast with the S-signal in Fig. 5. Now that φ_2 is advanced relative to φ_1 , it suffers a head-on collision with the cage, while this collision appeared cushioned by φ_1 in the prior. The timing between the packets appears to affect the system-bath chatter and the cross-communication between the coherent packets. Note such causality arises only in interpretation. Since the quantum propagator is linear in the Hamiltonian, the packets can be propagated separately and their joint action appears as interferences upon summation of complex amplitudes.

F. Heterodyned four-wave signal

In Figure 11, we have also provided a cut from the degeneracy window. This signal rides on a constant background, which is present at negative time due to probe scatter from the permanent volume grating. The baseline is drawn to show the negative dips, which arise from interference between the π -phase shifted resonant FWM signal and the instantaneously diffracted probe pulse. Only polarization that radiates within the probe pulse and falls in the degenerate window can produce this heterodyned signal. Radiation after finite time evolution on the E-state cannot interfere with the probe and appears as the positive valued signal. We note the gentler decay of the coherence at degeneracy, an effect that can be ascribed to the cross-correlation of packets that record a similar history in the bath.

G. Selection by the environment: Arrested dissipation in a quiescent cage

The analysis above was based on experiments with the narrow band pulses shown in Fig. 3. We consider the effect of increasing the initial energy separation between packets, $\lambda_1 = 540$ nm and $\lambda_2 = 560$ nm, and using broader spectra, $\text{fwhm} = 20$ nm and 25 nm, respectively. The probe is not altered. Now, the AS-window is centered at 485 nm. To the extent that the initial energy ordering is maintained, $\bar{\varepsilon}_1 - \bar{\varepsilon}_2 > 0$, the AS-signal should appear to the blue of the probe window at 500 nm.

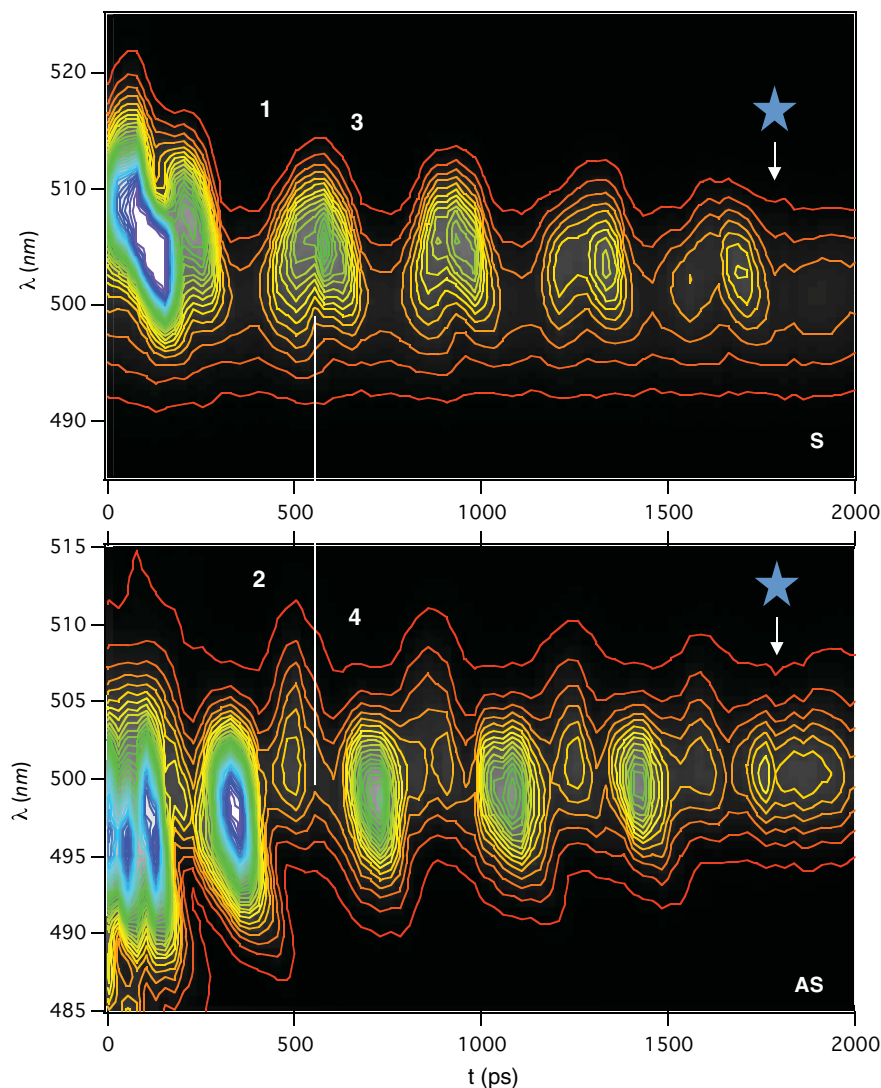


FIG. 9. The same experiment as in Fig. 3 (S, top; AS, bottom), but with φ_2 launched ahead of φ_1 : with $t_{21} = 70$ fs (100 fs time difference in t_{21}). The S-signal tracks φ_2 as it turns the corner (1–3), while the AS-signal captures φ_1 at large phase angles (2, 4). The outer contour profiles can be compared with the intensity plots in Fig. 5, they show the same cage modulation. The stars mark the abrupt decoherence, when the signal drops to the energy diagonal of Fig. 8.

In Figure 12, we show the λ, t_{31} -image of the AS-signal, at the nominal $t_{21} = 0$ value, which is assigned to the time that maximizes the first blue-shifted recursion. The scattering at $t_{31} = 0$ is in the proper AS-window. The spectrum upon first recursion is significantly narrowed and shows both red and blue wings – the coherence is between packets that overlap in energy. The insets in Fig. 12 clarify the connection between the colors and their counter phase timing – red at p^+ , blue at p^- . Following the insets, the off-diagonal energy distribution can be read-out from the spectral shifts: the red-shift defines the width of energy overlap ($\varepsilon_{2,\max} - \varepsilon_{1,\min}$), while the blue-shift defines the outer separation ($\varepsilon_{1,\max} - \varepsilon_{2,\min}$). The packets were initially prepared with $\omega_1 - \omega_2 = 650$ cm^{-1} , and $\Delta\omega = 800$ cm^{-1} . By the second recursion ($t_{31} \sim 600$ fs), the observation of 8 nm and 10 nm red and blue wings establishes that the signal is limited to packets in which $\bar{\varepsilon}_1 - \bar{\varepsilon}_2 = 100$ cm^{-1} , and $\Delta\varepsilon_1 \sim \Delta\varepsilon_2 \sim 350$ cm^{-1} . The spectral cuts show that the blue wing decays rapidly, in three cycles, while the cage-modulated red-wing amplitude decays with the predissociation of the population.

Past 1.2 ps, the blue wings disappear, signifying that now the coherence is limited to a narrow band in energy, with $\bar{\varepsilon}_1 - \bar{\varepsilon}_2 < 0$.

The observed periods taken from the spectral cut at 505 nm is shown in Figure 13. A gentle modulation of the period by the cage motion, also apparent in the modulation of signal amplitudes in Fig. 12, is observed. Based on the Morse decomposition (right ordinate in Fig. 13), φ_2 was launched with an initial vibrational energy of 2450 cm^{-1} . The periods, which can only be extracted after a cycle of motion, show coherent motion that starts at a significantly lower energy and remains in a ~ 500 cm^{-1} band, with no evidence of dispersion. The observable energy loss is no more than the modulation amplitude. The contrast with respect to dispersion of the observed periods in Fig. 7 is dramatic. Even though φ_1 is now launched at higher energy, and therefore suffers a more violent collision with the cage, the observable coherence shows a gently driven cage that it follows with dissipation nearly arrested. The dissipation rate of the superposition is significantly less than what is observed for individual packets

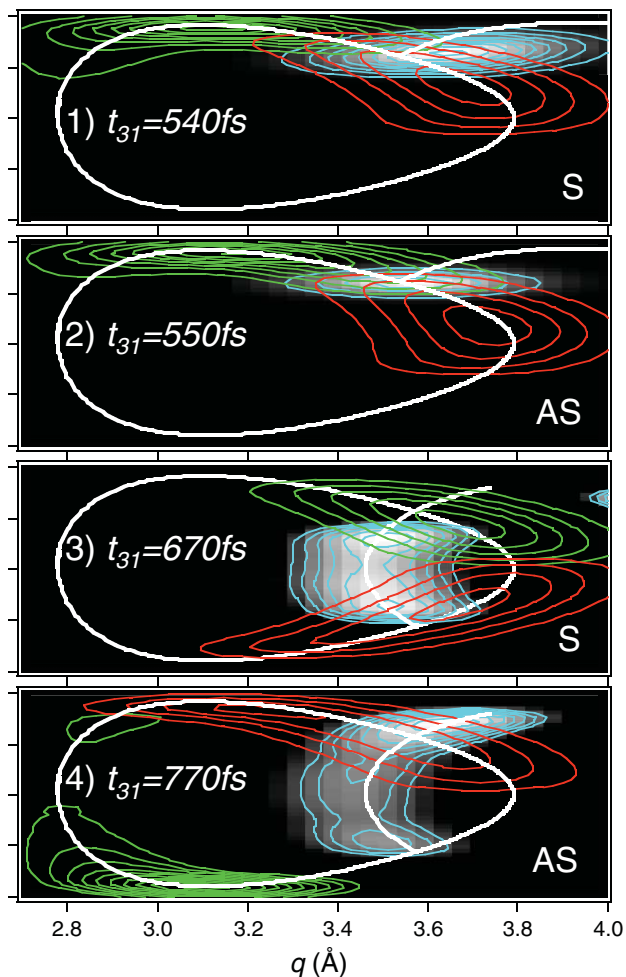


FIG. 10. The synchronization required to form the signal in Fig. 6 can be understood using classical trajectory ensembles to represent packets. We show the two circulating packets (red, green) captured at the identified t_{31} times, which correspond to the four marked events in Fig. 9, along with the E-state packet (blue) formed by the interception of φ_2/φ_1 by the FC window carved in time by the probe pulse to generate the S-/AS-scattering cases, respectively. The trajectories are propagated on a Morse potential, and the effect of the environment is only taken into account as an energy dependent dissipation.

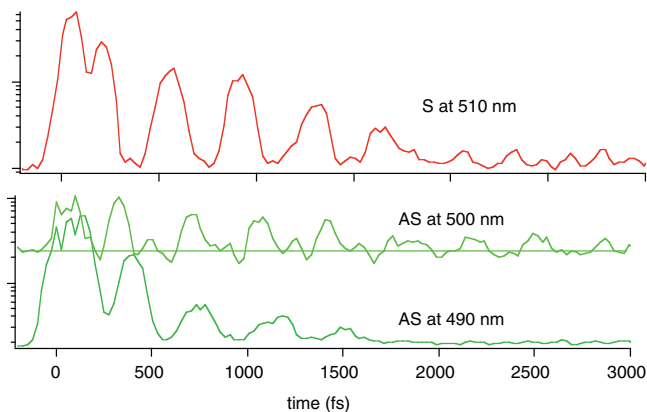


FIG. 11. Spectral cuts from Fig. 9, at the indicated wavelengths. The AS-signal in the degenerate window is on a constant background due to the permanent volume grating burned in the sample. The negative dips arise from the heterodyned signal.

extracted from pu-pr periods (Fig. 7). Although the spectral widths of the preparation pulses were more than tripled, the resulting coherence is locked in a narrow energy band, between $\nu = 15$ and 20. Evidently, the suddenly driven cage selects the part of the system that can follow it coherently.

H. Two-time correlation

By selecting a detection wavelength, the signal can be represented in a two-time t_{21}, t_{31} -correlation map, as in Figure 14. These can be regarded as the timing of the selected differential scattering process, or as the cross-correlation of packets in phase space. The general features of the signal can be reconstructed according to Eq. (15), using trajectories on a Morse potential, as shown in the inset. The reproduction quantifies our discussion of the measurement in Sec. II, otherwise it is simply another representation of the data. In the absence of dissipation and dephasing, a set of such measurements is sufficient to reconstruct the system Hamiltonian.³⁶ The same is not possible here. A strategy to develop an atomistic picture of the underlying quantum coherent dynamics would be through semiclassical forward simulations.

The two-time maps establish the coherence memory of the system, i.e., its dependence on the delay in launching times of the two packets. This can be seen to be limited to one cycle of motion (~ 500 fs). The coherence decays if the second packet is launched after the first packet enters its second cycle of motion, after crashing against the cage. In essence, their interference is destroyed if separated by the reaction of the bath, but survives when both packets are involved in defining the bath reaction. Indeed, the short inter-packet memory could have been inferred from the absence of vibrational structure in the $B \leftarrow X$ absorption spectrum of iodine in rare gas matrices, what is associated with electronic dephasing, and has previously been explicitly treated through atomistic semi-classical dynamics.³⁷ This is to be contrasted with the case of Bromine in matrices, where vibrational structure can be seen in the Franck-Condon window, and also interferometric phase coherent dynamics of the molecule and the phonons can be demonstrated and controlled with time delayed, shaped pulses that act through the same $B \leftarrow X$ Franck-Condon window.^{16,20} The present measurements are for strictly vibrational coherence evolving on the excited electronic state, which cannot be observed in a frequency domain measurement. The measurements illustrate an important principle regarding coherent control in condensed media,³⁸ where despite electronic dephasing between ground and excited state, vibrational coherences survive and can be manipulated through excited state-excited state resonances (B-state and ion-pair state in the present).

I. Dependence on spectral overlap

The observable coherence, as measured by FWM, depends on the energy separation between the prepared packets. When prepared with narrow band pulses, the signal decays rapidly as the spectral overlap between preparation pulses is reduced. This is illustrated in Fig. 15, for two different

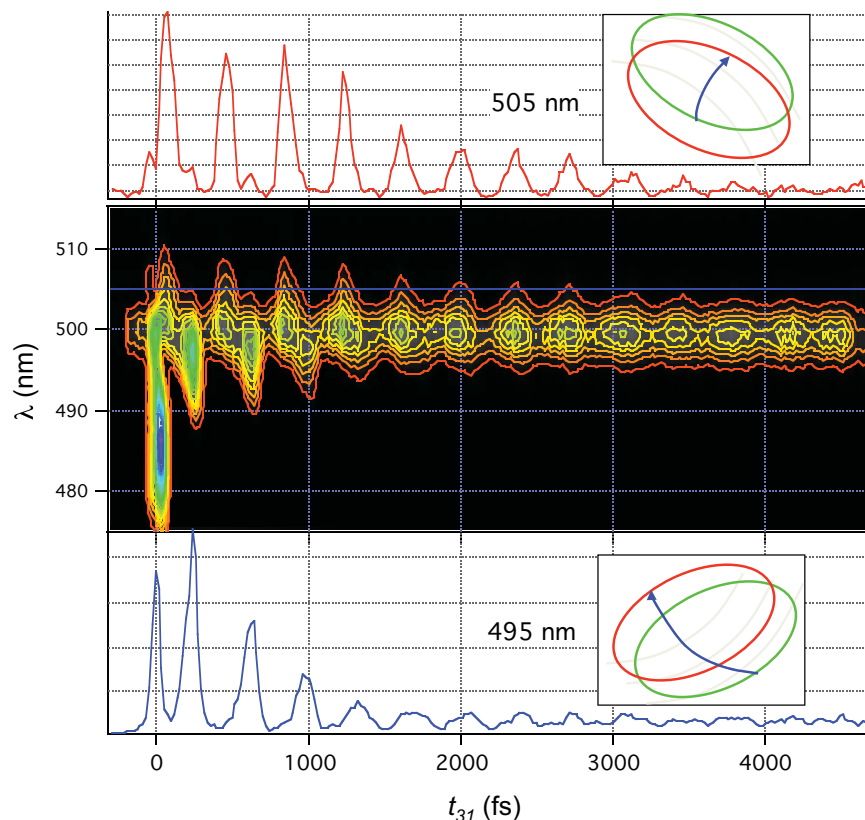


FIG. 12. AS-scattering obtained with pulse parameters $\lambda_1 = 540$ nm, $\lambda_2 = 560$ nm, and $\lambda_3 = 500$ nm, with bandwidths 20 nm, 25 nm, and 13 nm, respectively. The delay between packets is adjusted to obtain maximum signal at first blue recursion, and assigned $t_{12} = 0$. The red shift in the spectrum indicates energy overlap, while the decay of the blue-shifted peaks indicates non-linear dissipation and collapse of the anti-diagonal spread in energy. The cuts at $\lambda = 505$ nm and $\lambda = 495$ nm show the cage motion in their amplitude modulation. While the blue wing decays rapidly, the red wing decay is close to that of the population. The insets identify the phase space overlaps and projections that lead to the observed timing and color of the blue and red wings.

preparations: pulse spectra centered at $\lambda_1/\lambda_2 = 540/560$ and $545/560$ nm and probed at 500 nm. The signal could not be measured on further separating the pulse centers to $535/560$ nm. In the figure, the FWM signal and the pu-pr signal are

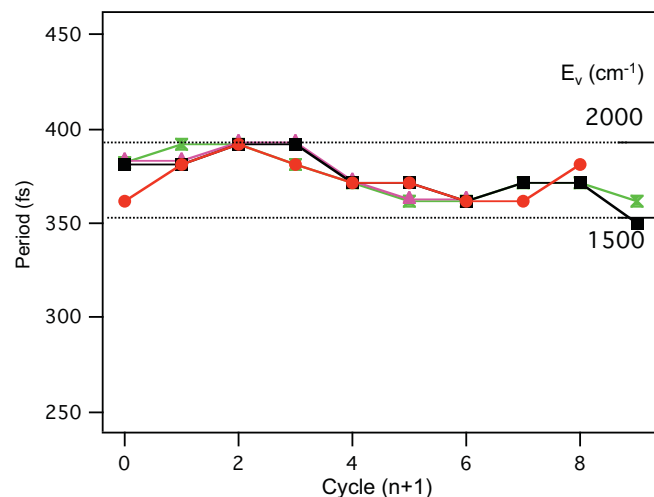


FIG. 13. Arrested dissipation. The periods collected from different t_{21} sets, extracted at 505 nm, show a perfectly correlated modulation that tracks the breathing of the cage. The vibrational energy of the molecule (right ordinate) remains within a narrow band of ~ 500 cm^{-1} , in stark contrast with that seen in Fig. 6.

normalized to the first recursion. By using the $t = 0$ response as reference, it is possible to compare the relative intensities at first recursion. The coherent signal drops by 50 between $540/560$ and $545/560$ preparations, while the spectral overlap drops by a factor of 5, consistent with the exponential sensitivity of the coherence to energy separation seen above.

The comparison between the FWM signal and the simultaneously recorded pu-pr signal provides a direct contrast between the classical and quantum coherence. In the pu-pr

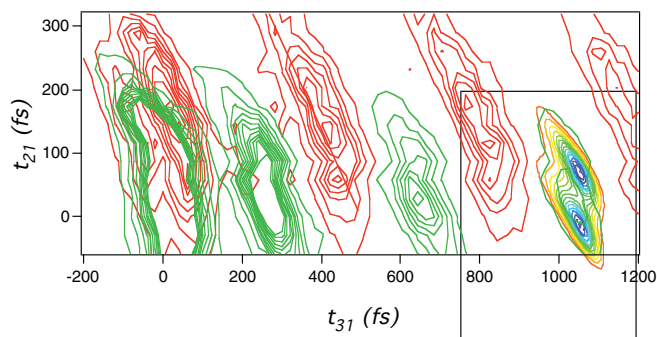


FIG. 14. Contour plot of the two-time correlation, at two selected wavelengths: AS at 485 nm (green), and S at 504 nm (red). The ordinate, t_{21} , is the delay between packets, while the abscissa, t_{31} is the probe time. Overlaid on the last AS-recursion is the simulated signal, using Eq. (15) of text, assuming two Morse trajectories.

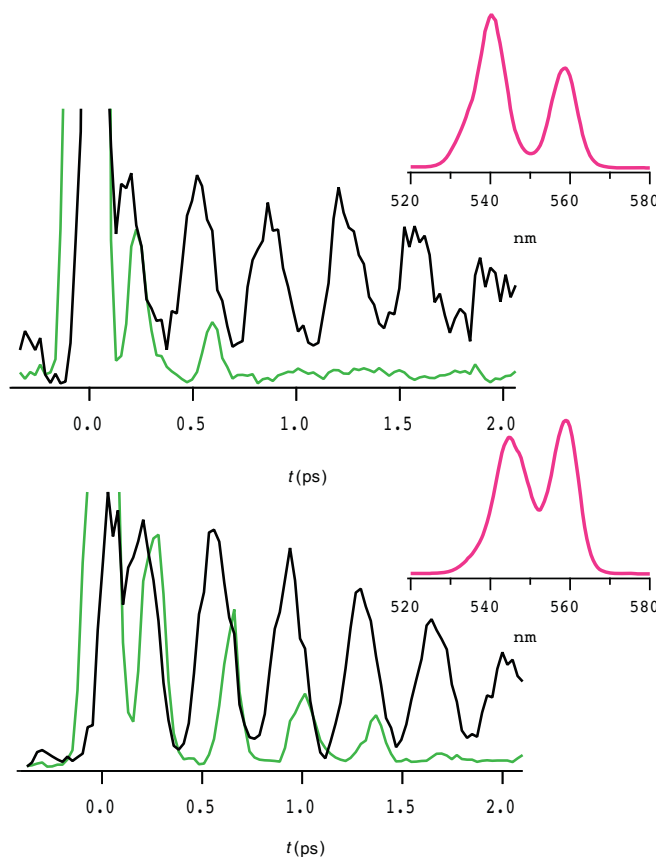


FIG. 15. Quantum versus classical coherence as a function of energy separation between preparation pulses. The FWM signal (green) and the simultaneously recorded pu-pr signal (black), detected through leaked LIF at 423 nm, are shown for two different pairs of preparation colors (purple): $\lambda_1/\lambda_2 = 540/560$ and $545/560$ ($\lambda_3 = 500$ nm, not shown). The signal amplitudes are normalized on the first recursion. The FWM signal, which measures the cross-coherence, decays rapidly as the spectral overlap between the preparation pulses diminishes. The pu-pr signal, which measures the classical coherence (diagonal bath), is not affected.

measurements, dispersion of the evolving packets leads to the dephased non-oscillating background that rises with time. The cross coherence signal occurs on a zero-background. The 540/560 preparation provides a clear contrast between measurements. While the pu-pr signal shows a density that oscillates for the duration of the excited state lifetime, the quantum coherence is lost after the second recursion, 0.6 ps. The measurements are carried out simultaneously on the same ensemble. The contrast can be understood by the fundamental difference: pu-pr measurements are diagonal in the bath (3), while the coherent FWM signal measures the off-diagonal of a system entangled with the bath (5b) and therefore decays with the bath-bath overlap.

IV. CONCLUSIONS

A principle aim of the present report is to outline electronically resonant four-wave mixing as a phase-space probe of vibronic coherences. We have presented selected measurements to highlight the information content that can be readily understood. Otherwise, the generated multi-dimensional data in these spectrally resolved, k-vector tagged, two-time correlations contains a large amount of detail. It should be possible, in principle, to reconstruct the dynamical states of the system from complete sets of two-time interferometric measurements.³⁹ Our implementation is designed to probe

manifestations of the quantum nature of mechanics in a molecular system that yields to atomistic interpretations and has previously been analyzed through classical mechanics. The experimental method, and the dissipative vibronic dynamics of I_2/Kr , map nicely on formal frameworks for quantifying and analysis of the emergence of classicality through decoherence.¹⁵ Instead of the often-necessary abstractions,^{12,40} the implementation realizes key principles in concrete molecular mechanical terms. We illustrate the contrast between classical and quantum coherence as a difference in measurement, through simultaneous pu-pr and FWM measurements of the same ongoing dynamics. We show that the data on a system strongly coupled to its environment naturally map out in energy representation – decoherence scales by the energy separation between off-diagonal densities. The connection with atomistic mechanics is most natural through semi-classical formulations, where decoherence of a quantum oscillator can be explicitly treated as irreversibility,⁴¹ as previously implemented on the same system.⁴² Quantum coherent dissipation, which corresponds to coherence transfer in state representation,⁴³ is demonstrated to imply non-locality, or equivalently, communication between packets through a common bath created by their action. This wave mechanics, when put in classical terms, appears as the simultaneous gain and loss of vibrational energy by one molecule or driving a local cage into dilation and following it adiabatically. Such

causality, and the notion of a back-action from the bath through which packets communicate, only arises in the translation to classical terms. Otherwise, in the full quantum evolution the surviving coherence is the interference between all paths. We see that rather than initial preparation, the observable post-dissipation coherence is selected mainly by the environment. When driving the environment by two packets that are further separated in energy, the coherence that survives is limited to a density entangled with a quiescent bath where dissipation rates are reduced. An even wider separation of initial energies leads to complete loss of the coherent FWM signal, while the classical measurement (diagonal in the bath) shows coherent oscillations that last the lifetime of the excited electronic state. It should then be clear that beside the energy separation between packets, the spectral composition of the pulses (pulse shapes) play a role in biasing the system-bath interaction. We take advantage of this consideration to prepare states with persistent coherence, which we will discuss in a follow-up report.

ACKNOWLEDGMENTS

The experimental part of this research was made possible under funding from USAFOSR Grant: FA9550-04-1-0186. It was completed under support from the National Science Foundation (NSF) Center for Chemistry at the Space-Time Limit, CHE-0802913.

- ¹D. Segale, M. Karavitis, E. Fredj, and V. A. Apkarian, *J. Chem. Phys.* **122**, 111104 (2005).
- ²S. Mukamel, *Principles of Nonlinear Optical Spectroscopy* (Oxford University Press, New York, 1995).
- ³N. Schwentner and V. A. Apkarian, *Chem. Rev.* **99**, 1481 (1999).
- ⁴D. Segale, PhD dissertation, University of California, Irvine, 2007.
- ⁵K. Ohmori, *Annu. Rev. Phys. Chem.* **60**, 487 (2009).
- ⁶M. Ovchinnikov and V. A. Apkarian, *J. Chem. Phys.* **106**, 5775 (1997).
- ⁷D. J. Tannor and S. Garashchuk, *Annu. Rev. Phys. Chem.* **51**, 553 (2000).
- ⁸Z. Ma and D. F. Coker, *J. Chem. Phys.* **128**, 244108 (2008).
- ⁹R. Zadoyan, M. Sterling, and V. A. Apkarian, *J. Chem. Soc. Faraday Trans.* **92**, 1821 (1996).
- ¹⁰M. Sterling, R. Zadoyan, and V. A. Apkarian, *J. Chem. Phys.* **104**, 6497 (1996).
- ¹¹A. Albrecht, *Phys. Rev. D* **46**, 5504 (1992).
- ¹²D. Giulini, E. Joos, C. Kiefer, J. Kupsch, I. O. Stamatescu, and H. D. Zeh, *Decoherence and the Appearance of a Classical World in Quantum Theory* (Springer, Berlin, 1996).

- ¹³R. T. Beyer, *Mathematical Foundations of Quantum Mechanics* (Princeton University, Princeton, NJ, 1955).
- ¹⁴A. Venugopalan, D. Kumar, and R. Gosh, *Physica A* **220**, 563 (1995).
- ¹⁵W. H. Zurek, *Rev. Mod. Phys.* **75**, 715 (2003).
- ¹⁶M. Guhr, H. Ibrahim, and N. Schwentner, *Phys. Chem. Chem. Phys.* **6**, 5353 (2004).
- ¹⁷M. Guhr, M. Bargheer, M. Fushitani, T. Kiljunen, and N. Schwentner, *Phys. Chem. Chem. Phys.* **9**, 779 (2007).
- ¹⁸M. Fushitani, M. Bargheer, M. Guhr, and N. Schwentner, *Phys. Chem. Chem. Phys.* **7**, 3143 (2005).
- ¹⁹M. Fushitani, M. Bargheer, M. Guhr, H. Ibrahim, and N. Schwentner, *J. Phys. B* **41**, 074013 (2008).
- ²⁰H. Ibrahim, M. Hejjas, and N. Schwentner, *Phys. Rev. Lett.* **102**, 088301 (2009).
- ²¹A. J. Leggett, *J. Phys.: Condens. Matter* **14**, R415 (2002).
- ²²A. Peres, *Phys. Rev. A* **30**, 1610 (1984).
- ²³W. H. Zurek, *Phys. Today* **44**(10), 36 (1991).
- ²⁴D. Cohen, *Phys. Rev. E* **65**, 026218 (2002).
- ²⁵G. A. Fiete and E. J. Heller, *Phys. Rev. A* **68**, 022112 (2003).
- ²⁶M. Bargheer, M. Gühr, P. Dietrich, and N. Schwentner, *Phys. Chem. Chem. Phys.* **4**, 75 (2002).
- ²⁷W. H. Zurek, *Prog. Theor. Phys.* **89**, 281 (1993).
- ²⁸T. Kiviniemi, J. Aumanen, P. Myllyperkio, V. A. Apkarian, and M. Pettersson, *J. Chem. Phys.* **123**, 064509 (2005).
- ²⁹This consideration is the basis of the principle of momentum filtering, previously demonstrated in time resolved CARS measurements.
- ³⁰S. Durr, T. Nonn, and G. Rempe, *Nature (London)* **395**, 33 (1998).
- ³¹M. Bargheer, P. Dietrich, K. Donovan, and N. Schwentner, *J. Chem. Phys.* **111**, 8556 (1999).
- ³²R. Zadoyan, M. Sterling, M. Ovchinnikov, and V. A. Apkarian, *J. Chem. Phys.* **107**, 8446 (1997).
- ³³The Morse parameters suitable for solid Kr are: $D_e = 6400 \text{ cm}^{-1}$, $\omega_e = 123.2 \text{ cm}^{-1}$, $\omega_e x_e = 0.593 \text{ cm}^{-1}$, and $T_e = 15400 \text{ cm}^{-1}$.
- ³⁴Z. Bihary, R. Zadoyan, M. Karavitis, and V. A. Apkarian, *J. Chem. Phys.* **120**, 7576 (2004).
- ³⁵V. Senekerimyan, I. Goldschleger, and V. A. Apkarian, *J. Chem. Phys.* **127**, 214511 (2007).
- ³⁶T. S. Humble and J. A. Cina, *Phys. Rev. Lett.* **93**, 060402 (2004).
- ³⁷M. Ovchinnikov and V. A. Apkarian, *J. Chem. Phys.* **105**, 10312 (1996).
- ³⁸T. Brixner, N. H. Damrauer, and G. Gerber, *Adv. At., Mol., Opt. Phys.* **46**, 1 (2001).
- ³⁹J. A. Cina, *Annu. Rev. Phys. Chem.* **59**, 319 (2008).
- ⁴⁰M. Razavy, *Classical and Quantum Dissipative Systems* (Imperial College Press, London, 2005).
- ⁴¹V. V. Dodonov, S. S. Mizrahi, and A. L. de Souza Silva, *J. Opt. B: Quantum Semiclassical Opt.* **2**, 271 (2000).
- ⁴²Z. Bihary, M. Karavitis, and V. A. Apkarian, *J. Chem. Phys.* **120**, 8144 (2004).
- ⁴³See for example, Y. Ohtsuki and Y. Fujimura, *J. Chem. Phys.* **91**, 3903 (1989).